3D modeling and experimental investigation on the damage behavior of an interpenetrating metal ceramic composite (IMCC) under compression

Joél Pascal Schukraft, Dominik Horny, Katrin Schulz, Kay André Weidenmann

Angaben zur Veröffentlichung / Publication details:

Schukraft, Joél Pascal, Dominik Horny, Katrin Schulz, and Kay André Weidenmann. 2022. "3D modeling and experimental investigation on the damage behavior of an interpenetrating metal ceramic composite (IMCC) under compression." *Materials Science and Engineering: A* 844: 143147. https://doi.org/10.1016/j.msea.2022.143147.

3D modeling and experimental investigation on the damage behavior of an interpenetrating metal ceramic composite (IMCC) under compression

Joél Schukraft [a,*], Dominik Horny [b,c], Katrin Schulz [b,c], Kay André Weidenmann [a]

[a] University of Augsburg, Institute of Materials Resource Management (MRM), Germany
[b] Karlsruhe Institute of Technology (KIT), Institute for Applied Materials - Computational Materials Science (IAM-CMS), Germany
[c] Hochschule Karlsruhe - University of Applied Sciences (HKA), Institute of Applied Research (IAF), Germany

1. Introduction

Continuously increasing demands on materials and the accompanying required environmental and economic benefit make the development of new composite materials necessary. By combining two different materials into one composite, the positive properties can be increased and the disadvantages of each material can be lessened. Choosing basic materials with a high recyclability or from a renewable resource and a cost-efficient manufacturing process, a promising alternative with enhanced properties can be developed. Combining two materials in an interpenetrating phase composite (IPC), so that both materials form a coherent phase – a ceramic and a light-weight metal for example – showed a great potential already in the early stage of development [1], as well as in the latest review publication [2]. Customizing the microstructure of the composite within experimental investigations showed that decreasing the pore size increases the mechanical properties [3]. Also for IPCs of different materials, as metallic glasses [4] or ceramic foams, used as a preform in the interpenetrating metal ceramic composite, this behavior can be observed for different pore sizes at a constant ceramic content [5]. But bringing materials with different properties together also raises a number of scientific questions concerning the damage behavior for example.

1.1. Related damage investigations in literature

For the presentation of the state of the art results given in literature, the focus lies first on the ceramic preform as the basic material of the composite and then is directed on a wider range of MMC foams. This finally leads to interpenetrating phase composites and the specific material combination of interpenetrating metal ceramic composites (IMCC) made from alumina and aluminum alloys.

Ceramic foams

In their fundamental studies, Ashby [6] and Gibson [7] derived a theoretical foundation for the mechanics of cellular materials. Using beam (and plate) theory, they derived dimensionless closed form relations between relative density of a foam and its mechanical properties. The resulting equations are able to describe the experimentally determined behavior of foams showing linear elastic, linear collapse or plastic response for a wide range of volume fractions with appropriately fitted proportionality factors. Colombo and Bernardo [3] showed, that in addition to the bulk density of open cell ceramic foams the pore size is also important for the mechanical behavior. They investigated the compressive strength of micro- and macrocellular foams (relative density $0.13 - 0.3$) with dense struts and cell sizes of 8 μm and $100 - 600\,\mu m$, respectively. As a result, the microcellular foams exhibited

* Corresponding author.
E-mail address: joel.schukraft@mrm.uni-augsburg.de (J. Schukraft).

https://doi.org/10.1016/j.msea.2022.143147

much higher compressive strengths (factor 3 – 4) due to the reduced probability of critical flaws in the ceramic struts with smaller cell size. The important aspect of flaws or residual pores within the ceramic has also been addressed by Studart et al. [8] who reviewed different processing routes of ceramic foams (replica, sacrificial templates and direct foaming) with respect to the microstructures and mechanical properties that can be achieved. Another key factor for the damage behavior of foams is the volume fraction of pores. In this regard, e.g. Meille et al. [5] investigated porous alumina ceramics, produced via gel casting, with a range of porosity between 30 and 75 % under uniaxial compression. The stages of damage and fracture were captured in in-situ compression experiments via X-ray computed tomography. They determined a change in damage behavior from brittle to cellular-like fracture for low porosity and high porosity foams, respectively.

MMC foams

A large variety of composite materials exists in between the range of ceramic foams and interpenetrating phase composites. For example Losch et al. [9] investigated an MMC foam based on magnesia partially stabilized zirconia particles and a stainless Cr–Mn–Ni TRIP steel. For damage analysis they used very similar analysis techniques as presented in this contribution: in-situ CT experiments were evaluated by using digital volume correlation (DVC) and local failure was derived from deformation field and correlated with the damaged microstructure. Berek et al. [10] used in-situ compression experiments in a X-ray computed tomography device to investigate the local deformation and the correlated phase transformation in the metallic phase of their MMC foam. Amsterdam et al. [11] investigated the fracture behavior of a foam, made of recycled MMC material (Al-9Si with 20 vol.-% SiC particles). Fracture was indicated at the Fe-rich plate-like precipitations, which dominated the damage behavior, as they span the entire cell wall thickness.

Interpenetrating phase composites (IPCs)

In the wide range of possibilities to combine IPCs from different basic materials, exemplary studies focusing on the damage behavior with at least one of the materials used in this study are presented in the following to show the state of research and the still remaining scientific questions:

Pezzotti et al. [12] for example investigated the fracture behavior of a hydroxyapatite polymer IPC and focused on macroscopic as well as microscopic mechanisms, such as crack-bridging. Ehrenfried et al. [13] investigated a degradable polymer–ceramic composite, made from beta-tricalcium phosphate and in-situ polymerized D,L-lactide. Qualitative X-ray micro-tomography measurements were taken to describe the failure in the composite. Crack initiation in the ceramic phase and crack-bridging of the ductile polymeric phase occurred. In the final stage of failure, debonding along the interface has been observed.

Y. Sun et al. [4] investigated an Mg-based metallic glass/titanium IPC regarding its mechanical properties in dependence of the metal content which varied between 30 and 70 % titanium. The compressive strength improved up to 44 % depending on the ratio between titanium and metallic glass. Fracture of the composite was investigated via SEM. For a low metallic ratio of 30 %, crack grow in the metallic glass matrix occurred axial to the load direction and lead to failure. For higher metallic glass volume ratios, long cracks at 45° to the loading direction developed and the brittle nature of the metallic glass was inhibited by the ductile nature of the metal.

Interpenetrating metal ceramic composites (IMCCs)

For IMCCs only a few investigations on the damage behavior have been published in literature. The material combinations and volume fractions as well as research objectives and methods vary strongly between the individual publications. Therefore, a direct comparison of these studies has to be conducted carefully, while considering the underlying conditions. In the following, state of the art investigations are presented in order of increasing metallic content:

L. Wang et al. [14] investigated a SiC/Al IPC with 20 Vol.-% metallic content and focused on the experimental and numerical simulation of three-point bending samples. In-situ SEM experiments were carried out to investigate the surface microstructure of the composite during failure. Cracks formed in the ceramic phase and propagation took place by micro-cracking under internal energy increase. The micro-cracks merged, and plastic deformation and failure of the aluminum phase took place, while a primary crack was formed and the internal energy dropped about 40 %. The primary crack partly propagated along the interface and crack bridging due to the ductile aluminum phase was observed.

F.-C. Wang et al. [15] investigated a similar SiC-based IPC under dynamic loading via a modified Split Hopkinsons Pressure Bar. The SiC skeleton was acquired with micro computed tomography and a 3D finite element model (FEM) was reconstructed from the scanning images. The damage evolution was studied and double cones were found under uniaxial dynamic compression. Damage initiation was determined by shear stress and damage zone extended along maximum shear stress direction. Only a few interactions of micro-cracks near the main cracks were recognized forming sample fragments. The same material system was investigated by Li et al. [16] under similar loading conditions, however, an interface model was included in the FE simulations. It became clear, that cracks initiate mainly within the SiC at the SiC/Al interface. Cracks propagated in the ceramic phase in compression direction and were deflected by interface debonding mechanisms before interconnecting with each other. Furthermore the Al phase absorbs 30% of the overall energy by plastic deformation but only 2% of its mass was lost due to damage.

Pezzotti et al. [17] investigated an Al_2O_3/Al IPC, with 30 % aluminum content. Based on their three-point fracture experiments, they investigated the toughening mechanism of the metallic phase, i.e. crack bridging. Residual stresses from infiltration process could be determined and were subtracted from the total stress at critical external load, to determine the net bridging stress. These were one order of magnitude above the bridging stress effect in monolithic alumina.

Scherm et al. [18] investigated an AlSi9Cu3/Al_2O_3 IPC with metal contents of 52 to 55 %. They investigated crack growth under compression and tensile conditions with ex-situ SEM investigation on the crack surfaces. For the ceramic content of nearly 50 % almost no macroscopic plastic deformation was visible. For tensile experiment a fracture plane perpendicular to the applied load occurred. Under compression the sample sheared in 45° direction. Microscopically, plastic deformation in the metallic phase was visible in dimples, with a diameter of 1 – 4 µm. A flaked structure occurred with furrows from ceramic particles, which slid between the two fractured halves. A strong interfacial adhesion was recognized, as no debonding occurred — not even in plastically deformed areas.

Agrawal et al. [19] investigated two metal–ceramic IPCs, based on copper and aluminum with an alumina ceramic phase. The fracture mechanism was studied in three-point bending tests in an in-situ ESEM setup as well as by computational modeling. Differences between the material combinations in crack propagation were determined considering thermal residual stress. For the Cu/Al_2O_3 IPC the crack propagated within the copper phase, as high thermal residual tensile stresses were measured in the 30 % metallic volume fraction. However, for the Al/Al_2O_3 IPC with 70 % metallic volume fraction, the cracks propagated within the ceramic phase, as the thermal residual tensile stress was smaller.

Roy et al. [20] investigated the internal load transfer under tension and compression on a interpenetrating MMC. They used an alumina preform fabricated via a poreformer and pyrolysis process infiltrated

with AlSi12 via squeeze-casting. For external stress, the load was transferred from the aluminum matrix to the silicon and alumina phase. The internal load in the alumina phase was found to be approx. double the externally applied load. Further studies of in-situ investigations of the internal load transfer of an lamellar metal ceramic composite can be found in Roy et al. [21,22]

As the summary of the state of the art shows, for IPCs with a dominant metallic content, especially IMCCs, only a few contributions on damage behavior have been published until now. As IMCCs have a complex microstructure, a 3D investigation of the damage is relevant and not satisfactorily elucidated so far. To the author's best knowledge, [15,16] are the only studies investigating an interpenetrating metal–ceramic composite ceramic content in 3D with both experimental and simulative methods. However, the material has a low metallic volume fraction of approx. 20% and was tested under dynamic loading conditions. This leaves a lot of room for questions concerning about the damage onset and progress for IMCCs with large metal contents (> 70%) under quasi-static loading.

Therefore, the combination of experimental and numerical investigations is used in this publication to investigate the damage behavior of an IMCC under compressive load three-dimensionally. In-situ computed tomography experiments combined with DVC evaluation, e.g. in F. Hild et al. [23] or Buljac et al. [24], are carried out experimentally, to investigate the microscopic as well as macroscopic damage behavior. From the reconstructed ceramic foam model, a FEM was applied and used to get a deeper understanding of the local crack initiation and formation in the ceramic foam as well as in the composite material, to make the damage behavior visible in the range from microscopical crack onset unto macroscopic failure of the IMCC sample. The mechanism of failure, not yet described in literature, will be investigated by combining both methods. The question of the possible partitioning of the damage process, with its detailed description in possible damage stages will be addressed.

2. Materials and methods

2.1. Materials and composite manufacturing

For investigation purposes, a macroscopically homogeneous and highly porous open-cell alumina ceramic preform with an approximate relative density of ca. 26 % is produced in these studies, which has been provided by Morgan Advanced Materials Haldenwanger GmbH, Waldkraiburg, Germany, holding a patent on the preform manufacturing process [25]. A slurry-based processing route is used to get a highly homogeneous ceramic preform: A stable ceramic foam suspension is produced by mechanical stirring. By stabilization via additives and a well-engineered drying process, the green body of the foam can be molded and dried without losing its fine and homogeneous porosity. Finally, the ceramic foam can be produced by sintering. A SEM image of the microstructure is given in Fig. 1a). The details of capturing are given in the image.

The IMCC was manufactured via gas-pressure infiltration with an AlSi10Mg alloy, based on the ceramic foam. The ceramic preform is heated up to 700 °C in an evacuated vacuum vessel at a residual pressure of maximum $2 \cdot 10^{-2}$ mbar with AlSi10Mg slabs. As the slabs are consequently melted and the melt surrounds the ceramic foam, an external Argon gas pressure of 60 bar was applied onto the surface of the melt bath. After a short dwell time of 10 min, the chamber was cooled down to room temperature under the remaining Argon pressure. After solidification, the infiltrated preform, i.e., the interpenetrating composite block, was removed from the pressurized vessel for sample preparation. Details and schematic drawing of the process setup are described elsewhere by the authors [26]. A SEM image of the micro structure is given in Fig. 1b). The details of capturing are given in the image. Further SEM images of the composite can be found in Horny et al. [26].

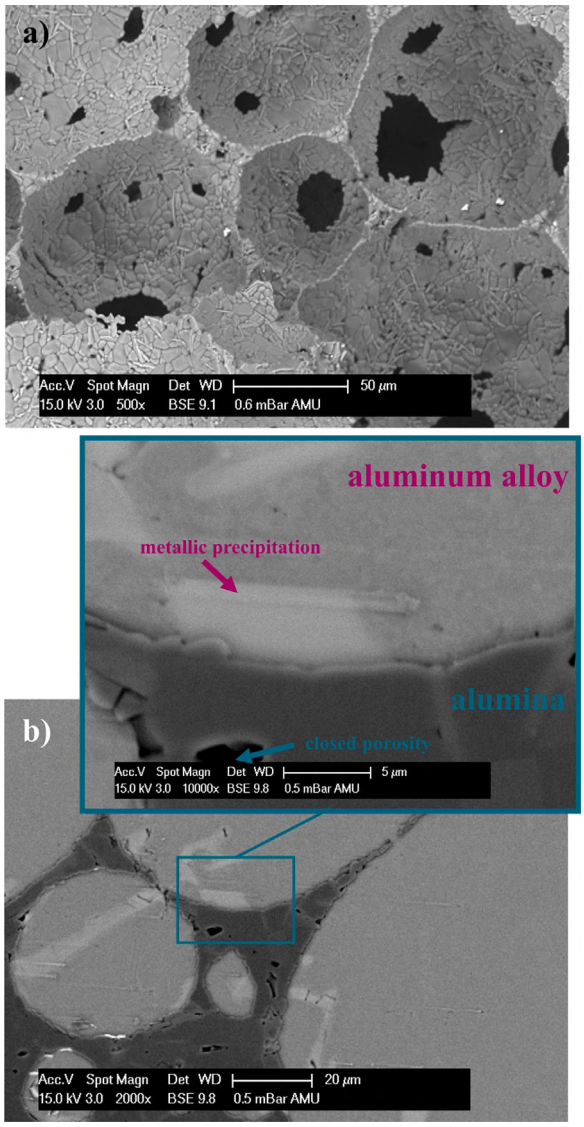

Fig. 1. SEM images of the alumina preform (a) and the infiltrated IMCC (b), captured under ESEM mode with 0.5 to 0.6 mbar of water pressure, 15 kV acceleration voltage and a spotsize of 3.0. Magnification and scale-bars are given in each image.

2.2. Sample preparation

For in-situ investigation, cylindrically shaped samples were prepared from the ceramic preform, as well as the IMCC. Therefore, a sample slice was cut out of a sample block of the ceramic foam and the composite with a cutting machine "Servocut® 301 - MA" by Metkon. With a diamond hollow drill, manufactured by Günther Diamantwerkzeuge and the dimensions of 3 mm as an outer diameter, cylindrical samples were cut out of the sample slice, according to given literature for other materials and dimensions, e.g. in Glinz et al. [27]. To reach plane parallel surfaces for compression testing, the cylinder faces were grinded parallel with abrasive SiC grinding paper of P500. The final sample size of the 3D in-situ investigated sample had a height of approx. 5.4 mm and a diameter of 1.87 mm for the ceramic preform, and 4.3 mm sample height and 1.75 mm in sample diameter for the IMCC. For experimental ex-situ investigations, cubic samples of the IMCC with an edge length of ca. 5 mm were used. Cutting was carried out with a diamond wire-saw by diamond wiretec and followed by grinding with SiC grinding paper step-wise from P320 to P800. The final dimension of the samples were measured with Tesa-μ-hite,

by Hexagon and surface parallelity brought to a maximum of 10 µm standard deviation.

2.3. Compression testing

For in-situ investigations, compression tests were carried out in a load stage inside the X-ray computer tomograph (CT) "Phoenix nanotom 180 m", by GE Sensing & Inspection Technologies GmbH. The load stage, with a maximum load of 25 kN in compression or tension, was designed and constructed at the Institute of Materials Resource Management at Augsburg University and has been described in detail by F. Thum et al. [28]. For compression testing, compression stamps were manufactured out of alumina rods with a diameter of 6 mm and the end faces have been polished. Regarding the investigation of the sample material, alumina suits best as compression stamp material because of the similar X-ray absorption behavior and the high hardness. The compression tests were realized by a stepper motor and controlled by a LabView program, which also records the data from the test (time and force-distance signal). The experiments were carried out travel controlled with a calculated nominal compressive strain rate of 10^{-3} 1/s. The calculation based on the rotation of the stepper motor, the belt ratio and spindle stroke. As the exact sample strain could not be determined with the in-situ testing setup used, the compression is given in mm for the in-situ experimental diagrams.

Load-steps were taken for the ceramic foam samples at 5, 9, 11, 16, 19, 21, 24, 29 and 33 MPa, as well as after failure. For the IMCC, load-steps were taken at 235, 280, 315, 335 and 370 MPa until reaching the maximum stress and five more load steps at 360, 290, 240 and 200 MPa afterwards, analogous to the results presented in [29], based on the same data. As the load steps are clearly visible in the stress–strain diagram and the strain could not be determined precisely enough from the in-situ testing setup, for comparison of the modeling results in the stress–strain-diagram with experimental data, ex-situ experiments were carried out with a universal testing machine of type 1464, with a load cell xforceK up to 50 kN, each of Zwick&Roell. Molybdenum sulfide (OKS Spezialschmierstoffe GmbH) was used as a solid lubricant between the sample and the stamps in accordance to DIN 50106 [30]. A preload of 20 N was applied onto the sample, before the data logging started. The experiments were also carried out travel controlled with a calculated nominal compressive strain rate of 10^{-3} 1/s. The elastic part of the curves were corrected based on elastic modulus measurements using ultrasonic phase spectroscopy [26].

2.4. X-ray computed tomography scanning parameters

For X-ray computed tomography, the highest possible resolution, regarding the diameter of the in-situ stage dimension was taken. The focus-object distance (FOD) was 13.8 mm and the focus-detector distance (FDD) 600 mm with a resulting voxel size of $(2.3\,\mu m)^3$. The software components Phoenix data sx2 acquisition and Phoenix data sx2 reconstruction were used to process the data and reconstruct a 3D image of the sample, each also by GE Sensing & Inspection Technologies GmbH. Further evaluations of the 3D images were carried out with the "Avizo" software by ThermoFisher Scientific. An evaluation path was defined and is described below in 2.5 "X-ray CT data evaluation".

Before sample loading, two CT scans and at each load step one CT scan were taken with a timing of 2000 ms, five averaged images at each position and 2000 positions/360°. To prevent large displacements of the sample and associated blurring during the CT-scan, the compression stamp position was held in position after reaching the load steps and during the scan. The scan was therefore started several minutes after reaching the load step, in order to relieve stress in the material due to plastic deformation and reach a stable condition. This is visible in the drops of the stress–strain curve at each load step in Fig. 7. The X-ray beam source was powered with 80 kV voltage and 180 µA current, compare Table 1.

Table 1
Parameter setting for the micro-computed tomography of the Al_2O_3 foam and the IMCC.

Parameters	Unit	IMCC	Ceramic foam
Voltage	kV	80	80
Current	µA	180	160
# of images	–	2000	1000
FOD	mm	13.9	13.9
FDD	mm	600	600
Voxelsize	μm^3	2.3^3	2.3^3

FOD: focus to object distance, FDD: focus to detector distance.

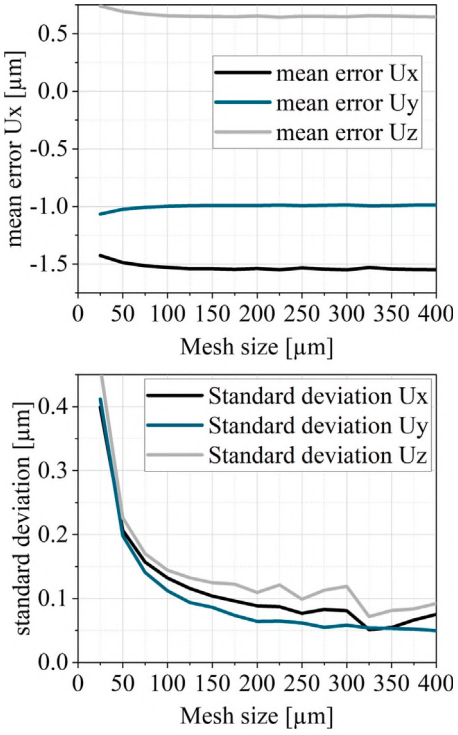

Fig. 2. Results of the *DVC uncertainty* module. Systematic error (top) and random error (bottom) of the displacement for the repeated, unloaded scan in a sub-ROI of the sample with a volume of 400 × 400 × 400 voxels.

2.5. X-ray computed tomography data evaluation

For data evaluation the "Avizo® software" by ThermoFisher Scientific and especially its DVC module was used. In the following, all Avizo® commands will be given in italic letters. For equal grayscale distribution in all scans, the *normalize of the grayscale* module was applied on every scan and gray values were distributed between 0 and 255 (8 bit). Then a sub-volume of the scan was extracted, which contained the relevant sample volume, to reduce the data storage requirements and shorten the calculation times. All regions of interest (ROI) (preload step scans as well as the scans at every load step) were rearranged with the function *register images* in an *iso-scale transformation* with *metric correlation* and the *quasi-newton optimizer* to compensate a possible shift of the sample between the scans. For all ROI identical positions, the scans were *resampled* and *interpolated* with a Lanczos algorithm [31]. The coordinate origin was set to one corner of the bounding boxes of all the ROIs uniformly. Then a mesh geometry was created for the ROIs and tested with different coarse mesh sizes according to [32]. With the *radial autocorrelation* module [33] an investigation on the correlation length of the microstructure was carried out and the precision of the correlation regarding the mesh size was controlled with the *DVC accuracy function*.

The *DVC uncertainty* module was used in a sub-ROI in the two unloaded sample scans to confirm the precision of the measurement and show its limits. An overview of the emphDVC uncertainty results is given in Fig. 2. The systematic error at the top of Fig. 2, caused by image acquisition and reconstruction, is constant and independent of the mesh-size. The random error, given on the bottom of Fig. 2 is caused within the DVC evaluation and dependent on the microstructure and correlation length. It decreases with an increasing mesh size. The developer of the commercial tool states, uncertainty below 0.1 voxel shows a good convergence and a suitable microstructure of the investigated material. As can be seen in Fig. 2, the uncertainty of the systematic displacement error lies beyond 1 μm, the random displacement error beyond 0.055 μm and the random error in E_{YY} strain beyond 0.04 voxel for the chosen mesh size of 350 μm.

The *DVC* module was successfully carried out in a *global DVC* approach, as all load-steps converged within the given range of 500 cycles. The undeformed sample scan was taken as reference volume for each load step and a global, finite-element-based approach was chosen. For details see [34]. The information received from the *DVC* module is the displacements and strains, the mesh of the data, as well as a residual file, containing the correlation residuals between the compared 3D images. Discontinuities in form of damage occur as extreme values (black and white) in the uniform scalar field of noisy grayscales of the residuals file [34]. To receive an DVC output of the undeformed sample, two scans were taken in the undeformed state of the sample and compared within the DVC module due to displacement and strain. This evaluation was also used, to check the influence of scan quality and artefacts on the DVC output and to validate the correct chosen input parameter of the *DVC* module. An *image stack process (ISP)* was used to separate the discontinuities of the residuals file and display them three-dimensionally in the sample ROI, to compare the strain-field E_{YY} in compression direction in the sample and the crack location.

3. Finite element modeling

Modeling and numerical investigations are carried out on the basis of the X-ray CT images described in Section 2.4. A cubic volume element with an edge length of approximately 1.9 mm in the center of a scanned $5 \times 5 \times 5\,\mathrm{mm}^3$ compression test sample was chosen as the ROI. In order to reconstruct the microstructure, ROI images were binarized, segmented and cleaned from segmentation errors. For a more detailed description of the segmentation routine we refer to [26]. Then, a cubic volume cutout with an edge length of 133 μm was chosen randomly within the segmented ROI, with the condition to match the overall ceramic volume fraction of 26%. Horny et al. [26] showed that the correct volume fraction is crucial for the mechanical response of both the foam and the composite. In the elastic range it is even more important than the size of the (representative) volume element. On this premise, a volume element size with an edge length of 133 μm was chosen as a compromise between accuracy and computational time.

The interface between the Al_2O_3 and the porous volume was triangulated and smoothened in order to reduce artificial stress concentrations in the FEM simulation, caused by the voxel discretized microstructure as shown in [35]. Therefore, a first order Laplacian algorithm implemented in the Materialize 3-matic 14.0 software [36] was used. For the numerical investigations of the foam and the Al_2O_3/AlSi10Mg composite, the ceramic as well as the metal volumes were meshed by tetrahedral elements. Finally, FE meshes were imported to *Abaqus 2020* [37] for further modeling and simulation. Mesh studies revealed that discretization effects are negligible for the chosen element size of approx. 3 μm. Exemplary structures for the foam and the composite are shown in Fig. 3.

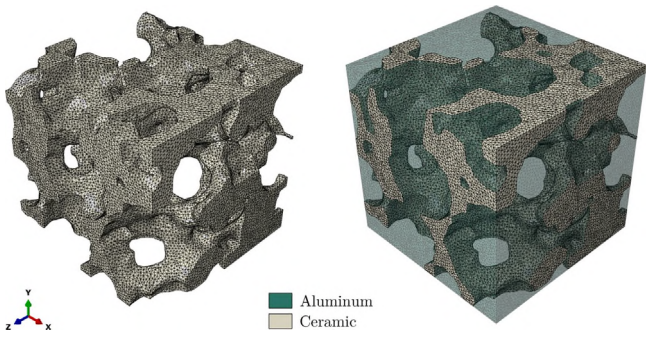

Fig. 3. Computational meshes of the ceramic foam (left) and the composite (right) used for the numerical modeling.

Table 2
Material input parameter. Tensile strength σ_t^I and yield strength σ_y are uniquely defined for the Al_2O_3 and the AlSi10Mg, respectively. Yield strength σ_y corresponds to yield stress at zero plastic strain $k(\bar{\varepsilon}_{pl} = 0)$.

Parameter		Unit	Al_2O_3	AlSi10Mg
Elastic modulus	E	GPa	350 [41]	70 [41]
Poisson ratio	ν	–	0.23 [41]	0.32 [41]
Tensile/yield strength	σ_t^I/σ_y	MPa	450 [42]	201.22 [43]
Fracture energy	G_f^I	$\mathrm{J\,m^{-2}}$	50 [41]	–
Hardening parameter	A	MPa	–	442.67 [43]
	ε_0	–	–	0.001 [43]
	n	–	–	0.112 [43]

3.1. Constitutive models

Linear elastic behavior of the Al_2O_3 ceramic was assumed up to the tensile strength σ_t^I. A Rankine damage initiation criterion was chosen to detect the onset of damage once the maximum principle stress σ_{max}^I exceeds σ_t^I. A regularized continuum damage model [38] with multi-directional smeared cracking assumption [39] accounts for the softening behavior and a linearly decreasing stress–displacement behavior was chosen. The relative displacement at which the stiffness reaches zero u_0 was determined by the fracture energy G_f^I and the tensile strength following Hillerborg [38]

$$G_f^I = \int \sigma_t^I \, du \rightarrow \; u_0 = \frac{2G_f^I}{\sigma_t^I}. \tag{1}$$

When reaching u_0, elements are deleted to avoid non physical distortions.

The AlSi10Mg was modeled using a linear elastic behavior followed by J_2 plasticity with isotropic hardening. It is described by the yield function

$$f(\boldsymbol{\sigma}, k) = \bar{\sigma} - k = 0 \tag{2}$$

containing the equivalent stress $\bar{\sigma} = \sqrt{3J_2}$ and the yield stress k. Here, J_2 represents the second invariant of the stress tensor. The evolution of k with respect to the equivalent plastic strain $\bar{\varepsilon}_{pl}$ is given by the Swift hardening law [40] reading

$$k(\bar{\varepsilon}_{pl}) = A(\bar{\varepsilon}_{pl} - \varepsilon_0)^n \tag{3}$$

with the hardening parameters $\{A, \varepsilon_0, n\}$. All relevant parameters are summarized in Table 2. For a detailed description of the constitutive models used for the Al_2O_3 and the AlSi10Mg, we refer to [35].

3.2. Boundary conditions

A compression load was applied on the volume elements of both the ceramic foam and the composite using rigid plates on top (moving) and on the bottom (fixed) to mimic the experimental test conditions (see

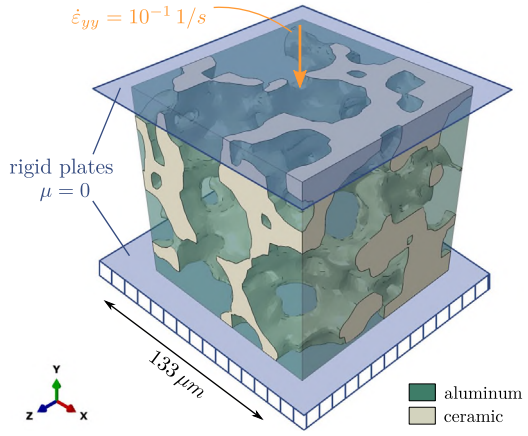

Fig. 4. Compression simulation boundary conditions. Same boundary conditions have been used for the ceramic foam and the MMC.

Fig. 4). No friction was assumed between the plates and the material (friction coefficient $\mu = 0$). Due to the good infiltration quality with low residual porosity (see Fig. 1) alumina and aluminum were considered to be perfectly tied at first approximation (see also [15,44,45]). As mechanical interface properties would have to be estimated due to the lack of reliable data we accepted the resulting overestimation of stresses and strength in this study. The volume elements are compressed in y-direction up to a total nominal strain of 2 % and 6 % in case of the ceramic foam and the composite, respectively. The strain rate of approx. $10^{-1}\,1/s$ is higher than in the experiments in order to save computational time. However, in convergence analyses a quasi-static response without any dynamic effects was observed at the chosen strain rate since only rate-independent constitutive models are used. Therefore, the higher strain rate compared to the experiments has no influence on the comparability of the results. The *Abaqus/Explicit* solver [37] using an explicit central difference time integration scheme was used to perform the simulations.

4. Results of the microstructural crack characterization

4.1. Ceramic preform

Based on the data from the micro-CT scans, the microstructure of the ceramic foam is reconstructed and modeled under uniaxial compression load within a FEM simulation as described in Section 3. The results given in Fig. 5 show the nominal stress–strain (top) response of the ceramic foam. Along the load history characteristic points (A–E) are highlighted in the diagram. At these points the development of the maximum principle stresses > 150 MPa (left), the crack strain magnitude (right) as well as the final damage pattern (bottom) in the microstructure is visualized with contour plots.

The macroscopic mechanical response of the ceramic foam under compression is (almost) linear for strains < 0.1%. Up to a stress of approx. 14 MPa, all deformations are linear elastic and concentrate at the top and the bottom of the spherical pore volumes as shown in the maximum stress distribution at point A. At the same point first damage initiates at multiple locations of high stress intensity as shown in the crack opening strain plot at A (right)).

The stress increases almost linearly up to 31 MPa at point B. The existing cracks grow in compression direction and the onset of new cracks can be determined (see B, right). The number of highly stressed locations increases, especially at the top and at the bottom of the pores and in small ceramic rods (B, left). The size of the highly stressed areas grows as well.

The foam exhibits a compressive strength of 51 MPa at a strain of 0.2% represented by point C. Cracks have opened and grown, mainly

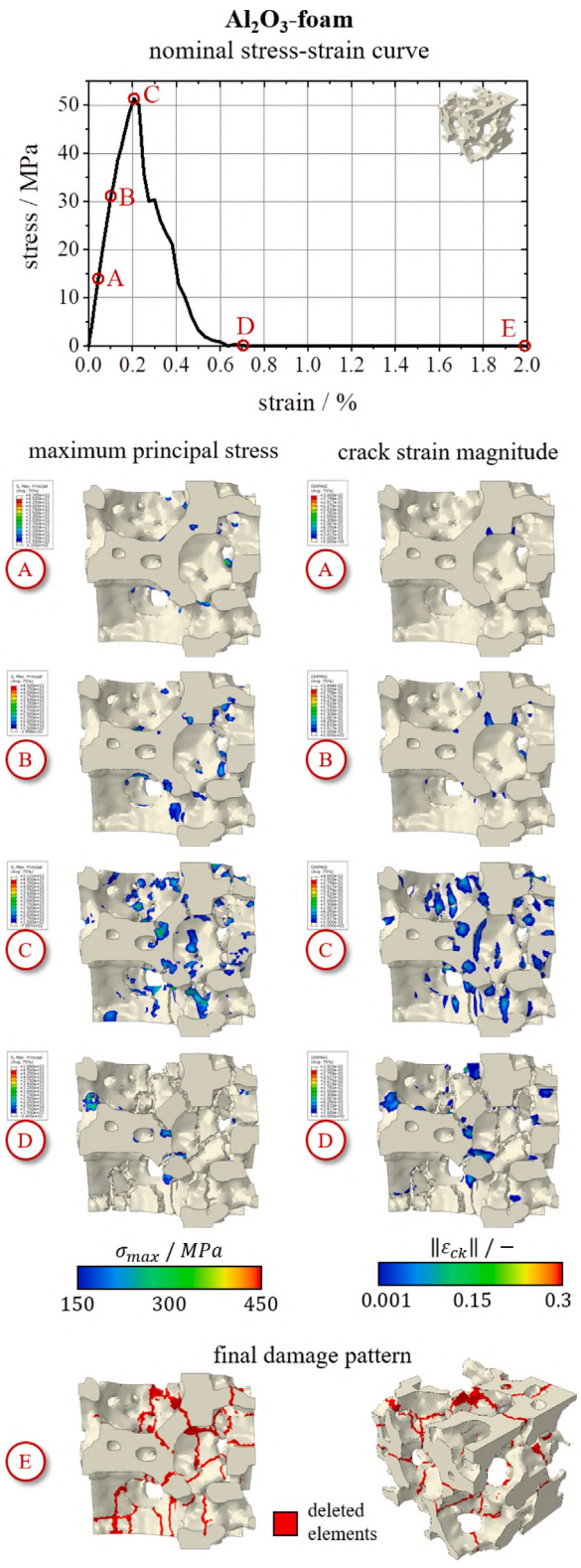

Fig. 5. Ceramic foam compression simulation results. Nominal stress–strain curve (top), evolution of maximum stresses (left) and crack opening strains (right) over the load history (A–D) and final damage pattern (E, bottom).

in compression direction but also diagonal and even perpendicular to it (cf. C, right). Maximum stresses occur mainly at the end of these cracks (cf. C. left). First elements are completely damaged and therefore

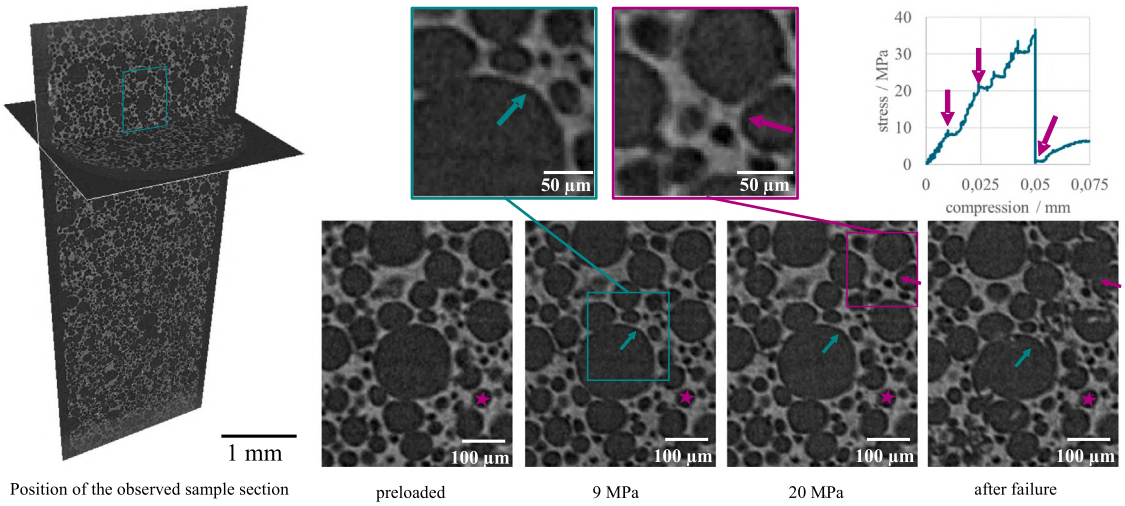

Fig. 6. In-situ compression testing results of the ceramic foam. Overview of the sample with marked section of the observed area (left). The respective stress–compression-diagram is given in the top right. The preloaded sample as well as 4 characteristic load steps are given and their position marked with arrows in the stress–compression-diagram. In the microstructural images pre-damage is marked with a star, crack onset of occurring damage is highlighted with arrows and a local enlarged view is given for the first time, the crack is visible. Scale-bars and stress level of each load steps are given respectively. The uniaxial compression direction is vertical in all images. (For interpretation of the references to color in this figure legend, the reader is referred to the web version of this article.)

deleted from the numerical model, in order to avoid non-physical distortions.

At approx. a 0.7% strain, the ceramic structure fails as it loses all load bearing capabilities. Stress concentrations in the ceramic dissolve (D, left) and a majority of the cracks opened up to the point of complete damage and the respective elements are eroded (D, right).

The resulting pattern of the completely damaged elements at the maximum total strain of the simulation (= 2%, see point E) is displayed at bottom of Fig. 5 in both side view and isometric view. Crack paths occur mainly in thin parts of the ceramic rods and the fraction of completely damaged ceramic volume is 7%. The cracks connect neighboring pore volumes and are not oriented in a specific direction with respect to the applied compressive load. Onset of cracking was detected in 25% of the ceramic volume.

The experimental results of the ceramic foam damage from in-situ X-ray computed tomography compression tests are given in the following: As Fig. 6 shows, crack formation and growth can be detected, but the width of the cracks is close to the spatial resolution. The 2D slices of the microstructure show the ceramic foam skeleton in light gray and its open porosity and the background in dark gray and black.

Manufacturing or preparation related pre-damage is visible in some regions of the sample volume, highlighted with the purple star in the preloaded image section Fig. 6. This pre-damage most likely contributes to the damage process in the ceramic foam, as it weakens the structure locally. However, in the displayed example the pre-damage cracks do not grow. They stay stable and are not part of the final macroscopic sample crack, as the load-step section after failure shows. At other locations, damage occurs already at low loading stresses of 9 MPa, as shown in the respective image section in Fig. 6.

The growing cracks are located close to the bottom and top of the pores in load-direction. With increasing load more cracks start to appear not only at the top and the bottom of the pores, but also at other locations (see Fig. 6, at 19 MPa).

As the bearable stress maximum of the sample is reached, a macroscopic crack forms through the sample and the sudden stress drop gets visible in the stress–compression-diagram in the top right of Fig. 6. The cracks in the ceramic phase unite and the sample fails. Because the sample strain could not be determined exactly with the used in-situ testing setup, the compression displacement in mm is given. The compressive stress strain behavior of this ceramic foam determined by a different test setup has been published elsewhere [43].

4.2. Composite

The microstructure of the IMCC is investigated experimentally by X-ray computed tomography at certain load steps as described in Section 2. Results of the macroscopic mechanical behavior and the microstructural damage onset and progress are shown in Fig. 7. A cut view of the 3D sample ROI is displayed for two different load-steps (2 at 280 MPa and 8 at 240 MPa) on the top left and right, respectively. For a closer investigation of the microstructural crack evolution, a 2D section of investigation is chosen within the ROI, marked by a green rectangle in the cut views. The load-steps taken during the experiment are given in the stress–displacement diagram in the top center of Fig. 7 and all load-steps are marked with numbers from 1 to 9. In the following these numbers will be used consistently for the description of the load-steps in the IMCC.

In the bottom row of Fig. 7, the 2D sections of the microstructure is given with scale-bars. Cracks are highlighted with arrows, where they can be observed for the first time. The ceramic phase in the composite is given in a lighter gray due to its slightly lower atomic mass than the metallic phase. The metal alloy is infiltrated into the spherical shaped pores of the ceramic foam, and is presented in darker gray values. Due to their similarity in X-ray absorption, the histogram peaks of the metallic and ceramic phase are melted into each other and cannot be separated without a big uncertainty in the local detection. Therefore, the original gray scale distribution of the scan is displayed in the Fig. 7. Porosity and cracks have gray values close to black. The white spots spread over the sample section represent the precipitates of the AlSi10Mg alloy and are highlighted by their high atomic mass in the imaging process by beam hardening artifacts. The precipitations contain heavy elements as iron (compare Cai et al. [46]), impurities of manganese and copper and other transition metals, as it is also given in the respective standard [47] for aluminum cast alloys, EN-AC43100.

As the section in the bottom row on the left at load-step 2 shows, the sample contains a low value of residual porosity within the ceramic phase. This is mainly closed porosity which is inaccessible for the melted metal during the infiltration process. Other defects occur in the metallic phase (blowholes) and at the interface (detachment effects) due to shrinkage of the AlSi10Mg during solidification.

In the image sections in Fig. 7, both kinds of defects can be seen in the larger metallic area in the lower middle of the section. First damage in this section-series is visible for load-step 3 at 315 MPa the upper left area in the ceramic phase, marked by the purple arrow.

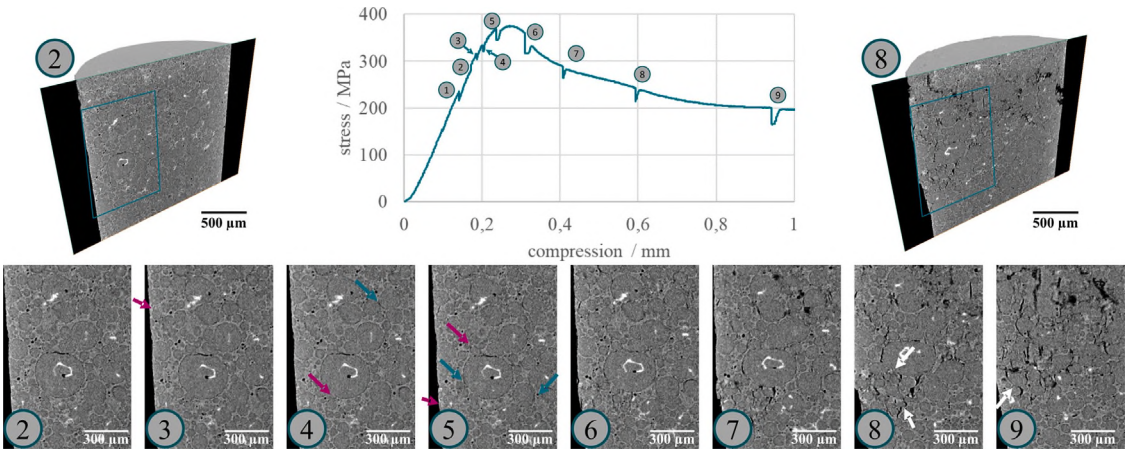

Fig. 7. Microstructural damage evolution within the interpenetrating composite during experimental in-situ X-ray computed tomography compression testing. An overview of the relevant sample ROI is given in the upper row for two different load-steps with the respective investigated section, presented in the lower row. stress–compression-diagram with all highlighted load-steps is given in the center. In the microstructural image sections in the lower row, purple arrows mark the location of cracks where they get visible the first time. Interfacial detachment is highlighted with green arrows and crack bridging with white arrows exemplary. The load-axis of the experiment is vertical in all given images. (Data based on the experiments, presented in [29], where the microstructure was investigated in a plane perpendicular to the load axis.) (For interpretation of the references to color in this figure legend, the reader is referred to the web version of this article.)

In load-step 4, further damage in the ceramic phase, close to the interface arises at 335 MPa and delamination of the interface gets visible in the upper region, highlighted with a green arrow. The crack initiated in load-step 3 grows in length and connects two metallic areas through the ceramic phase in load-step 4 (upper left region). In load-step 5, at 370 MPa close to the maximum stress, the crack in the upper left region (formed in load-step 3) still connects the metallic areas and becomes wider. Additional delamination at the interface takes place (green arrows), as well as new crack formation, predominantly in the ceramic phase (purple arrows).

In load-step 6, the stress-maximum is exceeded and a drop down to 360 MPa takes place. The crack in the upper left region (formed in load-step 3 in the ceramic phase) continues to grow at the interface between ceramic and metallic phase. Strong plastic deformation of the metallic phase sets in, as the larger metallic area in the lower middle shows. A relevant number of new cracks is formed over the sample section.

In load-step 7 shearing of the sample sets in and a further decrease in stress, down to 290 MPa, can be observed. This becomes visible in the section images. Parts of the original microstructure (c.f. load-step 6) are shifted out of the section, as it can be seen in the upper center of the section. The cracks in the sample seem to align mainly in load direction and start to unite in bigger cracks.

In load-step 8 further shearing of the sample, perpendicular to the section takes place and the cracks continue growing, uniting and becoming wider. Bridging effect of the spherical metallic phase sets in and forms interlocks at the interface, as the white arrows in the section show.

In load-step 9 the stress level decrease further to 200 MPa and a relevant part of the image section is littered with cracks. By shearing the main part of the original microstructure it is shifted out of the section, which is why the microstructural investigation is stopped at that load-step.

The IMCC was also modeled under uniaxial compression via FEM simulation as explained in Section 3. Fig. 8 and Fig. 9 show the results of the numerical investigations and the inner processes of the Al_2O_3 and the AlSi10Mg phase, respectively.

The nominal stress–strain behavior of the composite is displayed in Fig. 8 at the top and characteristic points are marked along the load history (A–F). Additionally, the development of the maximum principle stresses > 150 MPa (left), the crack strain magnitude (right) in the ceramic phase of the composite structure at these points as well as the final damage pattern (bottom) are presented. In Fig. 9 the evolution of the von Mises stresses > 200 MPa ($\approx\sigma_y$) and the plastic equivalent strains > 0.01 in the AlSi10Mg phase of the composite are displayed at the corresponding points (A–F) marked in Fig. 8.

For nominal compressive stresses < 190 MPa (below point A) the mechanical response of the composite is linear elastic. Areas of stress concentration in the ceramic can be found at the top and the bottom of the AlSi10Mg filled cavities (see Fig. 8, A, left) and first damage starts to occur in the ceramic at multiple locations at a load of approximately 190 MPa (see Fig. 8, A, right). In the aluminum phase, von Mises stresses exceed the yield strength of the material $\sigma_y \approx 200$ MPa at the interface close to the highly stresses areas of the ceramic phase, i.e. close to crack tips and at sharp ceramic edges, as presented in Fig. 9, A on the left.

Linear stress–strain behavior can be observed up to a load of 260 MPa, then the curve shown in Fig. 8 (top) kinks. At point B, which is chosen after the kink at a stress of 380 MPa, multiple cracks in the ceramic evolved mainly in compression direction but also diagonal and perpendicular to it at the interface to the AlSi10Mg phase (B, right). An increased number of well distributed areas with stress concentration can be seen throughout the whole ceramic phase (B, left). Plastic deformation and hardening in aluminum phase has taken place at this point, as represented in Fig. 9, B on the left. However, no equivalent plastic strain seems to be present according to image B on the right. This is a deception due to the chosen isosurface visualization style of the plastic strain and its bounds.

The compressive strength of 480 MPa is reached at a total strain of ≈1%, represented by point C in Fig. 8. The area and number of highly stressed locations increases further and becomes even more distributed (C, left). Cracks coalesce along the interface to the aluminum phase (C, right). In the right bottom corner of image C (right) branching of a crack can also be observed. In Fig. 9, C on the left side, shows how the Mises stress starts to concentrate from the left bottom to the top right corner. First isolated clusters of plastically highly strained areas can also be seen (C, right).

For strains > 1% softening of the composite due to damage of the ceramic can be observed as shown in Fig. 8 (top). At point D within this softening regime, the cracks are present in most of the ceramic areas at the interface to the AlSi10Mg phase (D, right). Multiple new cracks grow in compression direction starting at the top of the bottom left spherical aluminum filled cavity shown in Fig. 8, D (right). A concentration of damage in the ceramic can be observed from bottom left to top right corner of the investigated volume element. As displayed in Fig. 9, D (left), the von Mises stress increases further and concentration of the plastic strain in an 45° angle is observed (cf. D, right).

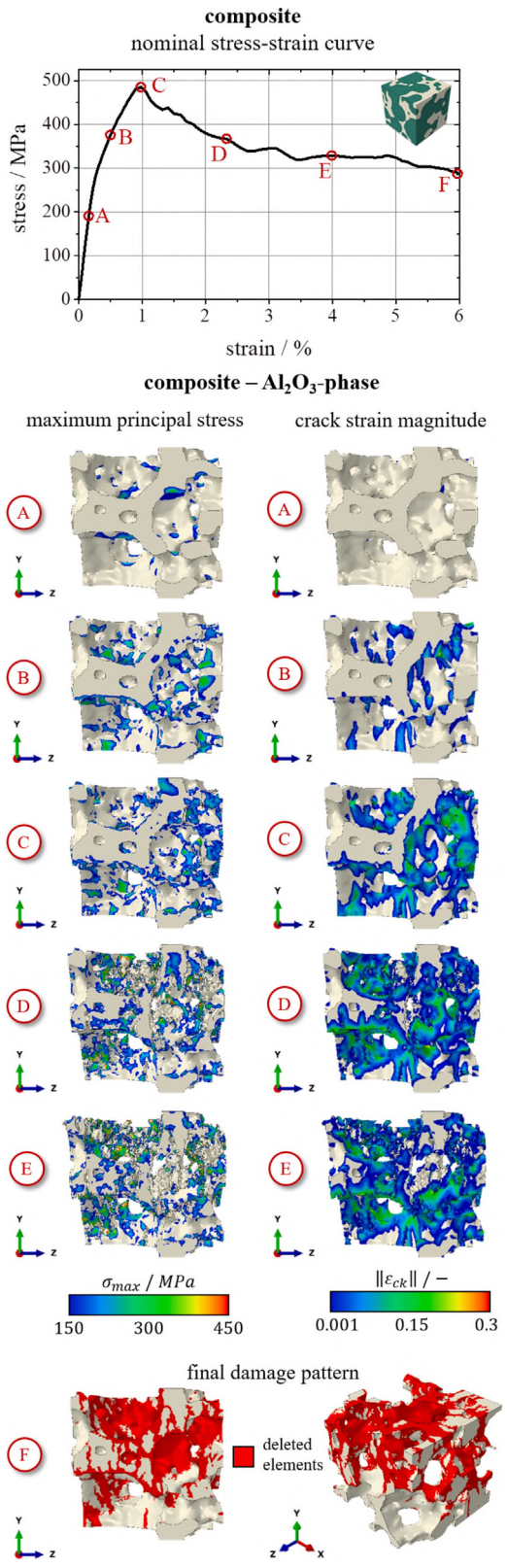

Fig. 8. Composite compression simulation results #1. Nominal stress–strain curve, evolution of maximum stresses and crack opening strains in the Al_2O_3-phase over the load history (A–E) and final damage pattern (F).

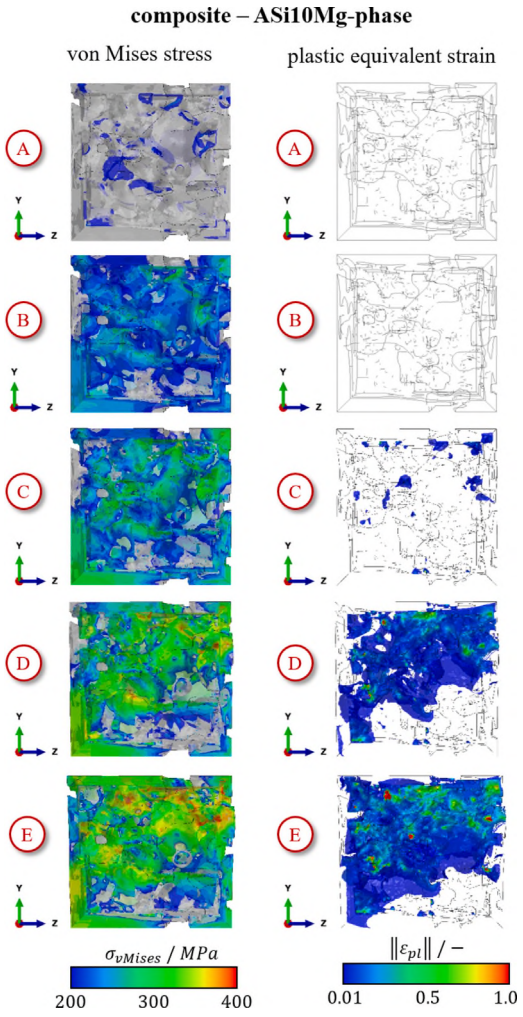

Fig. 9. Ceramic foam compression simulation results #2. Evolution of von Mises stresses > 200 MPa and equivalent plastic strain > 0.01 in the AlSi10Mg phase over the load history. The letters A–E correspond to the points marked in the stress–strain diagram given in Fig. 8.

At point E in the diagram (cf. Fig. 8), a plateau level of the composite residual strength is reached. Cracks are present in most of the Al_2O_3 structure (see E on the right). The lack of total interpenetrating connectivity in the ceramic leads to the loss of its load bearing capability. The AlSi10Mg phase mainly carries the mechanical load at this point leading to a shear dominated deformation as the distribution of the von Mises stress and the plastic equivalent strain in Fig. 9 E imply.

The damage pattern in the ceramic phase of the composite is shown in Fig. 8 at the ultimate strain of = 6% (marked as point F). At the bottom of the figure, this is displayed in both side view and isometric view. Cracked areas can be found mainly at the interface to the aluminum filled spherical cavities. Some further damage paths are oriented in compression direction as well as diagonal thin parts of the ceramic rods connecting the cavities. At point F 46.5% of the ceramic phase is completely damaged and crack onset is detected in almost 90% of its volume.

5. Determination of macroscopic failure mechanism

Besides the microscopic and local damage evaluation, the macroscopic failure behavior of the sample will be taken into account in the following, to get a better understanding of the material behavior under compression with regard to large scale and engineering components.

Digital Volume Correlations were carried out at the in-situ X-ray CT samples, to get a better understanding of the strain concentration

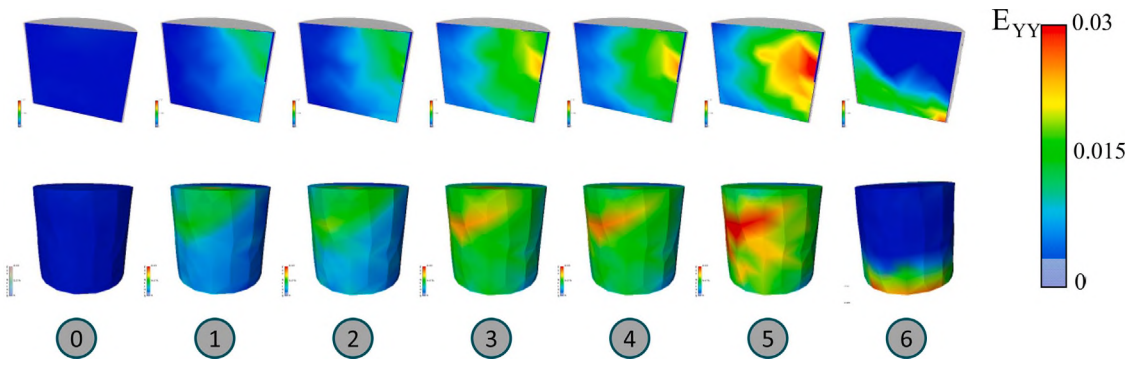

Fig. 10. Macroscopic evolution of the E_{YY} strain in compression direction detected with DVC for the unloaded sample up to first macroscopic shearing and corresponding stress and strain reduction in the unsheared sample regions at load-step 6, compare Fig. 7.) Upper row: Section through the IMCC sample, perpendicular to the maximum strain. Lower row: DVC mesh surface strain distribution. (Data based on the experiments, presented in [29]).

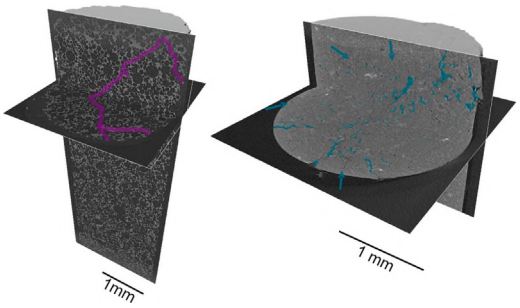

Fig. 11. Comparison of the damage pattern between the ceramic foam sample (left) and the IMCC sample (right) form in-situ X-ray computed tomography scans in the final damage step ("after failure" for the ceramic foam and "load-step 9" for the IMCC). For the ceramic foam the crack was highlighted manually in the slices. For the IMCC, an automated crack detection was used. Additional cracks which were not detected by the automated module were highlighted with green arrows. Scalebars are given for each sample, respectively.

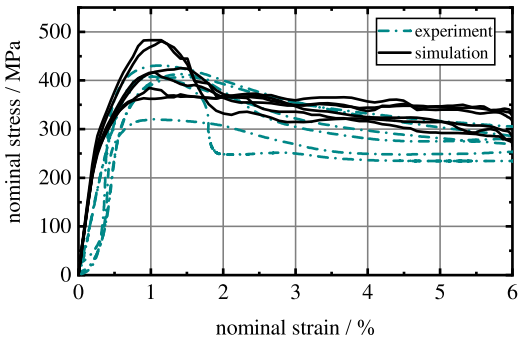

Fig. 12. Compressive stress–strain behavior of the composite determined by experiments (green, dashed) and simulations (black, solid).

in the respective state of testing. DVC investigations cover the range from the initial state of the compression test up to load-step 6, where the local stresses and strains are reduced by first macroscopic shearing. Fig. 10 shows cross-section as well as surface results for the strain in compression direction (E_{YY}) up to 3%.

For load-step 0, a scan repetition in the unloaded state was used, as described in Section 2.5. At load-step 0 the DVC shows homogeneous, undeformed strain values over the whole sample ROI.

For load-step 1 an increase in strain is visible in the upper area of the ROI (upper right corner in the upper row of Fig. 10) in a 45° angle to the load direction. In load-step 2 the strain increases over the whole ROI area and strain at the surface exceeds 1.5%, as depicted in the lower row of Fig. 10. For 315 MPa at load-step 3, the strain concentration on the mesh-surface increases distinctively in a crescent like structure at the surface. It spreads into the volume in a 45° angle towards the load direction as the cut view in the upper row shows.

For load-step 4 at 335 MPa and load-step 5 at 370 MPa, the crescent like local strain concentration increases further. For load-step 5 an additional strain increase in the opposite 45° angle becomes visible. The area of strain up to 3% enlarges inside the sample, as the section in the upper row of Fig. 10 shows. At load-step 6, after the stress maximum of the sample is exceeded (compare stress–compression diagram in Fig. 7) at 360 MPa, the strain decreases for the main part of the sample ROI. In the upper part of the ROI strains drop down to values close to 0% and in the lower half of the sample ROI to values close to 1.5%. Both regions are separated in an angle of approx. 45° which is clearly visible in the upper row of Fig. 10) at load-step 6.

For the subsequent load-steps 7–9 (compare stress–compression diagram in Fig. 7), the displacement of the sample get too large for the DVC module, as local displacements exceed the DVC correlation length. Thus, microstructural patterns of the sample cannot be assigned anymore.

Fig. 11 shows the damage patterns of the ceramic foam after failure (compare Fig. 6) and of the IMCC sample at the final load-step 9 (compare Fig. 7). An automated damage detection is not possible for the ceramic foam, due to the collapse of the pores by brittle failure. Consequently, a manual evaluation was carried out at the two cross-sections. For the IMCC, an automated evaluation procedure with the ISP tool is used as described in Section 2.5 instead.

For comparison of the macroscopic crack pattern, the ceramic foam will be included in this subsection, although the focus of it lies on the IMCC evaluation. In the ceramic foam the crack clearly divides the sample in a low number of fragments and runs fairly straight through the sample. Crack branching only takes place at two spots in the displayed sample sections. Shearing of the fragments can be observed after the crack has grown spontaneously through the whole sample dimension from one side to the other. In comparison to this, the damage pattern in the IMCC exhibits a broad crack distribution all over the sample diameter. Multiple crack branching points with parallel growing cracks and thin crack tips, which are undetectable for the automated evaluation module, are marked with green arrows. Crack paths through the ceramic phase, the interface and in some cases through the metallic phase as well as distinct cavities can be detected and thereby show the obvious change in damage mechanism from the ceramic foam to the IMCC.

To take an additional look on the IMCC macroscopic failure, the stress–strain diagrams from simulation and macroscopic compression tests at cubic samples (as described in Section 2.3) are compared with each other in Fig. 12. The results of six samples are displayed for both the experimental and numerical tests. Characteristic values are chosen to compare the results and to discuss the influence of different variables on macroscopic damage. In the elastic area the experimental

curves lie below the results from simulation. This is an effect of test setup compliance which could not be fully eliminated. Some of the curves even show a nonlinear behavior at the beginning due to gap closing effects. However, analysis of the curve slopes after this initial run in and experimental determination of the composite stiffness via ultrasound phase spectroscopy confirmed the stiffness determined in simulations [26].

For the nonlinear regime, the point at which an irreversible strain of 0.2% is present (analogous to the $R_{p,0.2}$ yield strength in tension) was chosen to compare the macroscopic stress. For experimental testing, the value extends from 303 MPa for a sample with high residual porosity to 368 – 398 MPa for the other tested samples. The values from simulated structures 317 – 368 MPa are found to be in good accordance with experimental findings.

The maximum stress is 391 ± 49 MPa in the experiment and 426 ± 55 MPa in the simulation and is located at a strain of approx 1%. After the peak-stress is visible in the experiments, the stress decreases from around 400 to 250 – 325 MPa. The simulative results show higher residual strengths in the range of 300 to 350 MPa. Furthermore, different types of stress drop can be observed. Two of the simulated structures do not show a pronounced stress decrease after reaching the maximum stress and maintain a high residual strength, whereas the other structures exhibit a clear drop. These different types are also found in the experimental compression tests.

6. Discussion

To get a detailed understanding of the IMCC damage behavior the microscopic as well as macroscopic results during compression, testing will be discussed, contrasted, and complementary phenomena will be brought together. A first look is taken at the damage behavior of the ceramic foam, to discuss the crack initiation and growth. In a second step we focus on the IMCC, to discuss the damage behavior on the basis of the ceramic foam damage. Similarities in the first stage of damage onset and differences in the further damage progression influenced by the interpenetrating metallic phase will be discussed.

6.1. Ceramic foam damage behavior

First, it has to be denoted that differences between the simulation and experimental results within the quasi-elastic area originate from artifacts of the experimental setup. Slightly unparalleled compression stamps, abraded ceramic particles or protruding edges at the sample specimen lead to inclines, stress concentration and local splintering. Additional holding steps under load, as they are used for CT scans during experimental testing can amplify the phenomena. This explains the differences in the curves between experiment and simulation, as all these effects are not taken into account and perfect sample and compression stamp geometries are assumed.

In both the in-situ experiment as well as the simulation of the ceramic foam under uniaxial compression, a step-wise increasing damage process can be detected. Cracks form preferably perpendicular to the inner surface at the open porosity, parallel to the load-direction in good agreement between modeling and experimental results. Simulations reveal stress concentrations at the top and the bottom of the spherical pores which are decisive for the onset of cracking as shown in Fig. 8 A and B. The location of these stress concentrations is a direct result of the geometrical arrangement of the ceramic and pores and agrees well with Kirsch's theory of stress distribution around a hole in a plate [48]. First cracks in the ceramic are observed at a macroscopic stress of 14 MPa, which seems to be within the linear elastic range of the stress strain behavior (see Fig. 8, top). The physical sample shows a certain amount of pre-damage, as the cross-sections in Fig. 6 visualizes. However, the pre-damage does not contribute to the final macroscopic damage, as a weaker failure plane exists in the ceramic foam. Nonetheless, it has to be considered, that small initial pre-damage cracks below the spatial resolution of the X-ray CT scans might be present and have an impact on the failure. However, they are not taken into account. Due to the brittle behavior in the experiment, the investigation of the ceramic foam in in-situ experiments is relatively elaborate and only certain snapshots of the damage state can be taken. In combination with the simulation of the reconstructed geometry, deeper insights into the damage behavior can be made.

With increasing load up to 31 MPa new cracks are formed, and existing cracks grow mainly in compression direction, as maximum tensile stresses are parallel to it (see Fig. 8 B). Bending stresses in the ceramic rods parallel to the compression direction grow with further increase of macroscopic strain. According to Ashby and Gibson [6,7] they are essential for the mechanical behavior of cellular solids foams. Between points B (31 MPa) and C (51 MPa) in Fig. 8 crack onset and propagation perpendicular and diagonal to the compression direction is observed as a result of the increasing bending stresses.

A spontaneous and brittle failure occurs in the weakest plane of the material structure in the experiment, as cracks in the ceramic struts grow from one to another pore. Although the ceramic foam has a high porosity content of approx. 74%, the experimental investigation does not show a pronounced cellular-like failure behavior as presented by Meille et al. [5] for highly porous ceramic foams. The final damage pattern of numerical investigations shown in Fig. 5 at point E reveals how cracks connect neighboring pores. Although a random orientation of cracks might be assumed at first sight, a preferred macroscopic orientation of cracks from bottom left to top right can be determined in image E (left), as well as in the left part of Fig. 11. This is an indicator for a mix between cellular-like and brittle damage characteristics. Due to the special morphology with small windows between neighboring pores and dense struts with a small amount of defects, the ceramic foam is rather comparable to closed-cell than to open-cell foams according to Studart et al. [8]. Therefore, it shows a high compressive strength compared to other foam manufacturing techniques (see Schukraft et al. [43] and compare Fig. 1a). With the higher mechanical strength, also a higher porosity ratio in the foam is necessary, to reach the brittle-cellular-like transition during compression failure.

It can be stated in a macroscopic consideration that the energy absorption of the highly porous ceramic foam during failure is higher in comparison to monolithic ceramics [49], but still low in comparison to damage tolerant materials, such as aluminum and its alloys, as for example the AlSi10Mg alloy EN AC-43000, see Schukraft et al. [43]. The damage pattern of the ceramic foam on the left side in Fig. 11 and picture E in Fig. 8 displays the final crack pattern. Cracks connect neighboring pores directly and a low proportion of crack deflection is present. This leads to a spontaneous failure and stress drop in the experiment (cf. stress–compression diagram in Fig. 6) and a stress loss in the simulation (cf. stress–strain diagram in Fig. 5 after the stress maximum in step C). Only a small fraction of approx. 7% of the ceramic volume is completely damaged and fully contributes to the energy absorption during damage at point E in the simulation.

6.2. IMCC damage behavior

In the IMCC the open porosity of the ceramic foam, as well as the openly accessible pre-cracks can be infiltrated with metal and consequently do not represent weakening points anymore. Besides that, the damage behavior can be significantly influenced by combining the two materials in an interpenetrating phase composite. For example, the IMCC shows a much more damage tolerant behavior than the brittle ceramic foam.

In this regard, the damage behavior on microstructural and macroscopic level will be the focus of the following comparison between experiment and simulation. Characteristic points along the stress–strain curve (see Fig. 12) are chosen to discuss microscopic and macroscopic damage phenomena and respective failure mechanisms of the IMCC. Three stages of damage are determined and will be further elaborated: the damage onset in the linear increase of the curve, the mechanism change around the stress maximum and the failure by shearing after the peak stress is exceeded.

6.2.1. IMCC damage onset

The experimental microstructural characterization of the composite shows first visible cracks at load-step 3 in the ceramic phase which implies a damage onset between 280 and 315 MPa. In previous investigation by the authors (see [29]) the first crack was visible between 235 and 280 MPa. In the simulation first cracks are already detected at stresses of approx. 200 MPa as depicted in Fig. 8 A (right). As shown in Fig. 9 (left) those first cracks are accompanied by plastic deformation in the metallic phase. The difference in damage onset can be explained by the restricted spatial resolution of the X-ray CT-scans. Cracks, interface detachments and infiltration defects with dimensions below 2.3 µm cannot be detected in the experiment. In accordance with the numerical results, cracks are forming in the ceramic phase close to the interface. This finding can also be confirmed by other studies of Al/Al_2O_3 composites [19]. To localize the early stage damage within the specimen, information on the macroscopic DVC deformation field was used (analogous to MMC foam investigations by Losch et al. [9]). In good agreement to their findings, the first detected crack in the microscopic analysis shown in Fig. 7 is located in the area where a high strain concentration was detected in the DVC analysis (cf. Fig. 10, load-step 3).

In comparison to previous investigation by the authors (see [29]) a first crack was visible between 235 and 280 MPa. Besides crack formation in the ceramic phase, interfacial detachment is also a significant fracture phenomenon in the damage onset stage between 235 and 335 MPa. In experimental investigations it especially occurs between 335 and 370 MPa and is clearly visible in the 2D images of load stages 4 and 5 in Fig. 7. Simulations yield similar results and allow for a comprehensive 3D analysis of the processes within the volume. Between point A (200 MPa) and B (380 MPa) in Fig. 8 cracks in the ceramic have grown both in compression direction and at the interface to the aluminum. The latter can be interpreted as an interface detachment mechanism. The increasing damage at the Al_2O_3/AlSi10Mg interface when reaching the compressive strength at point C becomes very clear in the visualization of the crack strain magnitude in Fig. 8. Up to this point plastic deformation in the AlSi10Mg increases also and the equivalent plastic strain locally exceeds 1% (cf. Fig. 9).

In experiments, the compressive yield strength (here defined as the point of a macroscopically irreversible compressive strain of 0.2%), varies between 303 MPa and 398 MPa. The values determined for simulated structures 317 – 368 MPa match quite well with experimental results and represent their lower range. Differences between experiment and simulation result from idealized model assumptions and uncertainties in determining the 0.2% strain values from experiments due to test setup compliance. As the macroscopic mechanical response of the ceramic foam in experimental investigations is almost linear up to failure (see Fig. 6), the IMCC also does not reveal a kink in the stress–strain curve before reaching the compressive strength (see Fig. 7). Therefore, the compressive yield strength of the composite is very close to the maximum compressive strength. However, as shown in Fig. 5 the non-linear behavior of the ceramic foam is more pronounced in the numerical analysis in the vicinity of the compressive strength. This leads to a stronger kinking in the stress–strain curve of the IMCC (see Fig. 8) which subsequently leads to decreased compressive yield strength values.

The DVC results in Fig. 10 are in good agreement with the local strain maxima from load-step 2 on at the sample surface observed in microstructural investigations. Strain grows in the inner of the volume and increase in the maximum value for the following load-steps 3 to 5, which explains the raise of the number of cracks, crack volume and the local strain, as given in Figs. 7, 8 and 9.

Similarities to the ceramic foam, when it comes to damage onset and propagation, are found as stress concentrations occur at the top and the bottom of the spherical cavities. However, due to the support of the aluminum phase, stresses are less localized in the ceramic phase of the composite compared to the foam (compare Fig. 8 A, left and 5 A, left). Therefore, macroscopic stresses and strains at first crack onset are increased by a factor of 10 and 3 compared to the ceramic foam, respectively. In the IMCC, a different behavior of crack initiation an propagation is observed due to the lateral confinement of the ceramic phase by the aluminum as described by [50]. The damage is much more distributed and at the maximum compressive strength at point C in 50% of the ceramic volume damage is already initiated, mainly due to the cracks close to the interface. However, only 2.3% of the ceramic is fully damaged, which is comparable to the foam at maximum compressive stress. As more damage energy is absorbed in the ceramic phase of the IMCC, the peak macroscopic stress and the corresponding strain can be increased by a factor of 7 and 3, respectively.

6.2.2. IMCC damage mechanism change

The first stage dominated by brittle behavior and a crack formation including onset of plasticity is followed by a second stage in which the damage mechanisms change to crack propagation and crack association unto dominance of plastic deformation. This second stage of damage includes the area around the stress maximum (see Fig. 12). In the final stress increase up to the maximum, a clear kink of the curve from the almost linear correlation between stress and strain is visible in experimental and simulated results (see Fig. 12 which already indicates some mechanism change).

First evidence for the introduction of a second damage stage is the change of the macroscopic strain distribution on the sample surface from load-step 4 to 5 (cf. Fig. 10). The former strain pattern not only widens and increases in its maximum value, but also forms a different shape. In load-step 5 in Fig. 10, the DVC results show a second branch of strain concentration in the opposite 45° angle to the load direction on the sample surface also the strain distribution inside of the sample changes significantly as presented in the upper row of Fig. 10.

The mechanism change is also observed in the microstructural investigation in Fig. 7. Between load-step 4 and 5 the formation of new cracks has finished and is not the dominant phenomenon anymore. However, with increasing compression crack propagation and association become dominant which can be seen in the image of load-step 6. In the simulations, this change in failure mechanism can also be observed. Starting from point C in Fig. 8, cracks start to grow and coalesce at the interface between ceramic and aluminum phase. Further, first plastically highly strained areas $> 1\%$ appear as shown in Fig. 9 C (right).

As the investigation of the quantitative crack evaluation with statistical analysis for the IMCC in Schukraft et al. [29] shows, the crack formation reaches a maximum between load-step 6 and 7 and a domination of crack volume increase sets in from that load-step on. This is confirmed by the simulative results of this studies, as at Point C in Fig. 8 50% of the ceramic volume crack onset is observed, however in only 2.3% of the ceramic volume cracks are open to full damage at u_0 (see Eq. (1)). The fraction of completely damaged ceramic increases to 25% at point D and 36.5% at point E whereas the overall cracked volume only increases to 57% indicating an damage behavior dominated by crack opening rather than new crack formation.

Another characteristic behavior in this damage stage is a strong decrease in strength after the stress maximum is exceeded. Experimentally, this could be observed in load-step 7 in Fig. 7, when shearing sets in. At this point, the resistance of the ceramic phase decreases significantly and plastic deformation of the metallic phase becomes dominant. This introduces the transition to the third and final damage stage in the experimental investigation.

6.2.3. IMCC failure by shearing

In this final damage stage, the metallic component becomes fully dominant and shearing of the sample in 45° angle to load direction sets in. The macroscopic strain distribution from DVC calculation indicates this outcome already in load-step 5 (see Fig. 10) and affirms this in load-step 6. Digital image correlation (DIC) at the surface of cubed

samples as well as the macroscopic crack pattern at the sample surface shown by [43] are confirmed by the 3D DVC investigation presented here.

The macroscopic shearing of the sample (see on the right of Fig. 11 and compare [29]), as well as the shearing on microstructural level in the experiment (see Fig. 7) and the simulation (see Figs. 8 and 9) can be observed in excellent agreement. In literature, such macroscopic shearing in a 45° angle toward load direction has been found by Sun et al. [4] for an interpenetrating composite of titanium and a brittle Mg-based metallic glass. The brittle nature can be inhibited by the ductile nature of the metal and lead to fail in graceful manner, as they state.

Closer look on the microstructure cross-sections of load-step 8 and 9 in Fig. 7 shows distinctive crack formation parallel to load-direction next to the macroscopic crack in 45° direction The high number of cracks contribute to the good-natured failure of the composite and to the high energy absorption of the composite during failure under compression. Another relevant mechanism, that contributes to the good-natured failure of the composite is the crack bridging of the ductile metallic phase. It can be observed in the final stage of damage, as it is highlighted with white arrows in Fig. 7 for load-step 8 and 9, as well as in the simulative results in Fig. 9 C on the bottom right corner of the structure. Besides, also debonding effects at the interface increase the damage tolerance of the composite (see Fig. 7). As already mentioned, the interface in the composite is not explicitly modeled in the simulation. Nevertheless, these debonding effects can implicitly be observed, as cracks in the ceramic phase of the IMCC grow predominantly at the interface to the AlSi10Mg phase (compare Fig. 8 F). All these phenomena occurring in the final stage of damage, result in the macroscopic behavior of a softening effect after the stress maximum with a decrease in stress. Due to the high metallic content the investigated IMCC retains a residual strength and stresses only decrease to a plateau level of 250 to 350 MPa.

6.3. Comparison to literature

Finally a last comparison to the literature should be made over the whole damage range and investigated methods: Independent of the composition of a ceramic phase with a metal or polymeric second phase, the IPCs begin to fracture within the ceramic phase under static load. Only one excerpt is given in literature with a Cu/Al_2O_3, investigated by Agrawal et al. [19]. An increase in damage tolerance is markable for brittle-ductile combinations of IPCs by crack bridging mechanisms. Ehrenfried et al. [13] for example describe this phenomenon for their ceramic-polymer interpenetrating composite. The ductile phase (polymeric or metallic) holds the composite together and bridges the crack in the ceramic phase — also compare the already mentioned literature by L.Wang et al. [14], Agrawal et al. [19] or Krstic [51], who first investigated the fracture of brittle-matrix/ductile-particle composites. In a further stage of damage, debonding effects between the two interpenetrating phases can take place. This is confirmed by the simulative, as well as experimental results (see Fig. 7) and in literature by Ehrenfried et al. [13] and L. Wang et al. [14].

In comparison to dynamic-load experiments, carried out by F.-C. Wang et al. [15] and Li et al. [16], parallels could be found in the damage behavior. In accordance with Li et al. cracks in the presented IMCC initiate mainly within the ceramic at the ceramic/aluminum interface. They also observed cracks propagating in the ceramic phase in compression direction first, which are then deflected by interfacial debonding mechanisms before interconnecting with each other. In their description of the phenomena, the Al phase absorbs most of the energy, once the ceramic phase lost its connectivity. This indicates a change in damage mechanism, as we found and describe it in this study. However, as the here investigated IMCC has a significant higher metal fraction, a residual strength is found after the damage of the ceramic, whereas the more brittle IPC in [15,16] loses all load bearing capacity. In conclusion, the here investigated material system shows improved damage tolerance due to the presence of a residual strength plateau, caused by crack bridging and the high metallic content.

7. Conclusion and outlook

In this study, advanced experimental and simulative methods were used to get a profound understanding of the damage mechanism in the investigated IMCC and the ceramic preform. As the first investigation of this kind of an IMCC with a high metal content and the consideration of the preform as well as the composite, the damage behavior under quasi-static load could be determined. The in total brittle damage behavior of the ceramic preform against the prediction of Meille et al. [5] was evidenced, regarding the highly durable microstructure. Damage onset in the ceramic struts parallel to compression direction could be explained by the fracture mechanics properties, regarding Ashby [6] and Gibson [7] and the suitable basis for a durable IMCC could be shown. For the IMCC the relevant damage progress could be described from first crack formation unto the final failure. As the investigations brought up, the IMCC fails in three main damage stages. Beginning with a damage onset stage, dominated by crack formation in the ceramic phase and at the interface and first plasticity, followed by a mechanism change, with crack clustering and increase of plastic deformation in the metallic phase. The final damage stage is dominated by shearing of the metallic phase, in formation of cracks and plasticity in one major shear plane. To the best of the authors' knowledge, this is the first time the damage behavior of an IMCC could be divided into different stages and the underlying mechanisms. In retrospect, the found damage stages can be transferred to other findings and literature.

For further investigations, it is planned to investigate the stiffness decrease linked to the damage onset. By cyclic unloading experiments and respective simulations the phenomena should be described quantitative in compression and tension experiments.

CRediT authorship contribution statement

Joél Schukraft: Conceptualization, Investigation, Writing – original draft. **Dominik Horny:** Methodology, Software, Writing – original draft. **Katrin Schulz:** Writing – review & editing, Supervision, Project administration. **Kay André Weidenmann:** Writing – review & editing, Supervision, Project administration.

Declaration of competing interest

The authors declare that they have no known competing financial interests or personal relationships that could have appeared to influence the work reported in this paper.

Data availability

The raw/processed data required to reproduce these findings cannot be shared at this time as the data also form part of an ongoing study.

Acknowledgments

The financial support for this work in the context of the DFG, Germany research projects SCHU 3074/1-1 and WE 4273/17-1 as well as the support by the European Social Fund and the State Baden-Württemberg, Germany is gratefully acknowledged. We want to thank Morgan Advanced Materials Haldenwanger GmbH for the friendly supply of complimentary preform material and Daniel Wegscheider for carrying out a part of the ex-situ compression testing experiments and his support with their evaluation.

References

[1] D.R. Clarke, Interpenetrating phase composites, J. Am. Ceram. Soc. (ISSN: 00027820) 75 (4) (1992) 739–758, http://dx.doi.org/10.1111/j.1151-2916.1992.tb04138.x.

[2] N. Kota, M.S. Charan, T. Laha, S. Roy, Review on development of metal/ceramic interpenetrating phase composites and critical analysis of their properties, Ceram. Int. (ISSN: 02728842) (2021) http://dx.doi.org/10.1016/j.ceramint.2021.09.232.

[3] P. Colombo, Macro- and micro-cellular porous ceramics from preceramic polymers, Compos. Sci. Technol. (ISSN: 02663538) 63 (16) (2003) 2353–2359, http://dx.doi.org/10.1016/S0266-3538(03)00268-9.

[4] Y. Sun, H. Zhang, A. Wang, H. Fu, Z. Hu, C. Wen, P. Hodgson, Compressive deformation and damage of mg-based metallic glass interpenetrating phase composite containing 30–70 vol% titanium, J. Mater. Res. (ISSN: 0884-2914) 25 (11) (2010) 2192–2196, http://dx.doi.org/10.1557/jmr.2010.0272.

[5] S. Meille, M. Lombardi, J. Chevalier, L. Montanaro, Mechanical properties of porous ceramics in compression: On the transition between elastic, brittle, and cellular behavior, J. Eur. Ceram. Soc. (ISSN: 09552219) 32 (15) (2012) 3959–3967, http://dx.doi.org/10.1016/j.jeurceramsoc.2012.05.006.

[6] M.F. Ashby, Mechanical properties of cellular solids., Metall. Trans. A, Phys. Metall. Mater. Sci. (ISSN: 03602133) 14 A (9) (1983) 1755–1769, http://dx.doi.org/10.1007/BF02645546.

[7] L.J. Gibson, M.F. Ashby, The mechanics of three-dimensional cellular materials, Proc. R. Soc. London. A. Math. Phys. Sci. 382 (1782) (1982) 43–59, [Online]. Available: https://www.jstor.org/stable/pdf/2397268.

[8] A.R. Studart, U.T. Gonzenbach, E. Tervoort, L.J. Gauckler, Processing routes to macroporous ceramics: A review, J. Am. Ceram. Soc. (ISSN: 00027820) 89 (6) (2006) 1771–1789, http://dx.doi.org/10.1111/j.1551-2916.2006.01044.x.

[9] K. Losch, K. Schladitz, U. Ballaschk, H. Berek, C.G. Aneziris, Interrupted in-situ compressive deformation experiments on mmc foams in an XCT: Experiments and estimation of displacement fields, Image Anal. Stereol. (ISSN: 1580-3139) 33 (2) (2014) 131, http://dx.doi.org/10.5566/ias.v33.p131-145.

[10] H. Berek, U. Ballaschk, C.G. Aneziris, K. Losch, K. Schladitz, The correlation of local deformation and stress-assisted local phase transformations in MMC foams, Mater. Charact. (ISSN: 10445803) 107 (2015) 139–148, http://dx.doi.org/10.1016/j.matchar.2015.06.020.

[11] E. Amsterdam, Babcs&aacute, n. Norbert, J.T.M. de Hosson, P.R. Onck, J. Banhart, Fracture behavior of metal foam made of recycled MMC by the melt route, Mater. Trans. (ISSN: 1345-9678) 47 (9) (2006) 2219–2222, http://dx.doi.org/10.2320/matertrans.47.2219.

[12] G. Pezzotti, S. Asmus, Fracture behavior of hydroxyapatite/polymer interpenetrating network composites prepared by in situ polymerization process, Mater. Sci. Eng.: A (ISSN: 09215093) 316 (1–2) (2001) 231–237, http://dx.doi.org/10.1016/S0921-5093(01)01250-3.

[13] L.M. Ehrenfried, D. Farrar, D. Morsley, R. Cameron, Mechanical behaviour of interpenetrating co-continuous b-TCP-PDLLA composites, Key Eng. Mater. 361–363 (2007) 407–410, http://dx.doi.org/10.4028/www.scientific.net/KEM.361-363.407.

[14] L. Wang, Q. Fan, G. Li, H. Zhang, F. Wang, Experimental observation and numerical simulation of SiC3D/Al interpenetrating phase composite material subjected to a three-point bending load, Comput. Mater. Sci. (ISSN: 09270256) 95 (2014) 408–413, http://dx.doi.org/10.1016/j.commatsci.2014.08.008.

[15] F.-c. Wang, X. Zhang, Y.-w. wang, Q.-b. Fan, G.-j. Li, Damage evolution and distribution of interpenetrating phase composites under dynamic loading, Ceram. Int. (ISSN: 02728842) 40 (8) (2014) 13241–13248, http://dx.doi.org/10.1016/j.ceramint.2014.05.031.

[16] G. Li, X. Zhang, Q. Fan, L. Wang, H. Zhang, F. Wang, Y. Wang, Simulation of damage and failure processes of interpenetrating SiC/Al composites subjected to dynamic compressive loading, Acta Mater. (ISSN: 13596454) 78 (2014) 190–202, http://dx.doi.org/10.1016/j.actamat.2014.06.045.

[17] G. Pezzotti, O. Sbaizero, Residual and bridging microstress fields in Al2O3/Al interpenetrating network composite evaluated by fluorescence spectroscopy, Mater. Sci. Eng.: A (ISSN: 09215093) 303 (1–2) (2001) 267–272, http://dx.doi.org/10.1016/S0921-5093(00)01844-X.

[18] F. Scherm, R. Völkl, A. Neubrand, F. Bosbach, U. Glatzel, Mechanical characterisation of interpenetrating network metal–ceramic composites, Mater. Sci. Eng.: A (ISSN: 09215093) 527 (4–5) (2010) 1260–1265, http://dx.doi.org/10.1016/j.msea.2009.09.063.

[19] P. Agrawal, C.T. Sun, Fracture in metal–ceramic composites, Compos. Sci. Technol. (ISSN: 02663538) 64 (9) (2004) 1167–1178, http://dx.doi.org/10.1016/j.compscitech.2003.09.026.

[20] S. Roy, J. Gibmeier, V. Kostov, K.A. Weidenmann, A. Nagel, A. Wanner, Internal load transfer in a metal matrix composite with a three-dimensional interpenetrating structure, Acta Mater. (ISSN: 13596454) 59 (4) (2011) 1424–1435, http://dx.doi.org/10.1016/j.actamat.2010.11.004.

[21] S. Roy, J. Gibmeier, A. Wanner, In situ study of internal load transfer in a novel metal/ceramic composite exhibiting lamellar microstructure using energy dispersive synchrotron X-ray diffraction, Adv. Eng. Mater. (ISSN: 14381656) 11 (6) (2009) 471–477, http://dx.doi.org/10.1002/adem.200800352.

[22] S. Roy, J. Gibmeier, V. Kostov, K.A. Weidenmann, A. Nagel, A. Wanner, Internal load transfer and damage evolution in a 3D interpenetrating metal/ceramic composite, Mater. Sci. Eng.: A (ISSN: 09215093) 551 (2012) 272–279, http://dx.doi.org/10.1016/j.msea.2012.05.016.

[23] F. Hild, A. Bouterf, L. Chamoin, H. Leclerc, F. Mathieu, J. Neggers, F. Pled, Z. Tomičević, S. Roux, Toward 4D mechanical correlation, Adv. Model. Simul. Eng. Sci. 3 (1) (2016) http://dx.doi.org/10.1186/s40323-016-0070-z.

[24] A. Buljac, C. Jailin, A. Mendoza, J. Neggers, T. Taillandier-Thomas, A. Bouterf, B. Smaniotto, F. Hild, S. Roux, Digital volume correlation: Review of progress and challenges, Exp. Mech. (ISSN: 1741-2765) 58 (5) (2018) 661–708, http://dx.doi.org/10.1007/s11340-018-0390-7.

[25] O. Lavrentyeva, Verfahren zur herstellung von aufgeschäumten keramischen Werkstoffen sowie dadurch herstellbarer keramischer schaum: DE, 2016, DE102015202277A.

[26] D. Horny, J. Schukraft, K.A. Weidenmann, K. Schulz, Numerical and experimental characterization of elastic properties of a novel, highly homogeneous interpenetrating metal ceramic composite, Adv. Eng. Mater. (ISSN: 15272648) 1901556 (2020) http://dx.doi.org/10.1002/adem.201901556.

[27] J. Glinz, D. Kytýř, T. Fíla, J. Šleichrt, A. Schrempf, D. Fürst, J. Kastner, S. Senck, In-situ compression test of artificial bone foams in controlled environment using X-ray micro-computed tomography, Acta Polytech. CTU Proc. 25 (2019) 48–51, http://dx.doi.org/10.14311/APP.2019.25.0048.

[28] F. Thum, P. Potstada, M.G. Sause, Development of a 25kN In Situ load stage combining X-Ray computed tomography and acoustic emission measurement, Key Eng. Mater. 809 (2019) 563–568, http://dx.doi.org/10.4028/www.scientific.net/KEM.809.563.

[29] J. Schukraft, C. Lohr, K.A. Weidenmann, 2D and 3D in-situ mechanical testing of an interpenetrating metal ceramic composite consisting of a slurry-based ceramic foam and AlSi10Mg, Compos. Struct. (ISSN: 02638223) (2021) 113742, http://dx.doi.org/10.1016/j.compstruct.2021.113742.

[30] DIN Deutsches Institut für Normung, Prüfung metallischer Werkstoffe - Druckversuche bei Raumtemperatur, Beuth Verlag GmbH, Berlin, 2016.

[31] C. Lanczos, An iteration method for the solution of the eigenvalue problem of linear differential and integral operators, J. Res. Natl. Bur. Stand. 45 (1950) 255–282.

[32] F. Hild, in: ThermoFisher Scientific (Ed.), Generate a DVC Mesh of Complex Shapes, 2019, [Online]. Available: https://xtras.amira-avizo.com/xtras/tutorial-generate-a-dvc-mesh-of-complex-shapes.

[33] K. Madi, S. Gailliègue, M. Boussuge, S. Forest, M. Gaubil, E. Boller, J.-Y. Buffière, Multiscale creep characterization and modeling of a zirconia-rich fused-cast refractory, Philos. Mag. (ISSN: 1478-6435) 93 (20) (2013) 2701–2728, http://dx.doi.org/10.1080/14786435.2013.785655.

[34] K. Madi, G. Tozzi, Q.H. Zhang, J. Tong, A. Cossey, A. Au, D. Hollis, F. Hild, Computation of full-field displacements in a scaffold implant using digital volume correlation and finite element analysis, Med. Eng. Phys. 35 (9) (2013) 1298–1312, http://dx.doi.org/10.1016/j.medengphy.2013.02.001.

[35] D. Horny, K. Schulz, Analysis of interpenetrating metal ceramic composite structures using an enhanced random sequential absorption microstructure generation algorithm, J. Mater. Sci. (2022) http://dx.doi.org/10.1007/s10853-022-07180-1.

[36] Materialise N.V., 3-matic, 2019, [Online]. Available: https://www.materialise.com/software/3-matic.

[37] Dassault Systèmes, Abaqus 2020, Simuilia Corp., Providence, RI, USA, 2019, [Online]. Available: https://www.3ds.com/products-services/simulia/products/abaqus/.

[38] A. Hillerborg, M. Modéer, P.E. Petersson, Analysis of crack formation and crack growth in concrete by means of fracture mechanics and finite elements, Cem. Concr. Res. (ISSN: 00088846) 6 (6) (1976) 773–781, http://dx.doi.org/10.1016/0008-8846(76)90007-7.

[39] J.G. Rots, J. Blaauwendraad, Crack models for concrete: discrete or smeared? Fixed multi-directional or rotating? Heron (ISSN: 00467316) 34 (1) (1989) 3–59.

[40] H.W. Swift, Plastic instability under plane stress, J. Mech. Phys. Solids (ISSN: 00225096) 1 (1) (1952) 1–18, http://dx.doi.org/10.1016/0022-5096(52)90002-1.

[41] ANSYS, Inc., Ansys granta EduPack, 2020, [Online]. Available: www.ansys.com/materials''.

[42] T. Hoshide, H. Sugiyama, Numerical analysis of sample-size effect on strength of alumina, J. Mater. Eng. Perform. (ISSN: 10599495) 22 (1) (2013) 1–8, http://dx.doi.org/10.1007/s11665-012-0214-3.

[43] J. Schukraft, C. Lohr, K.A. Weidenmann, Mechanical characterization of an interpenetrating metal-matrix composite based on highly homogeneous ceramic foams, in: J.M. Hausmann, M. Siebert, A. von Hehl, K.A. Weidenmann (Eds.), Hybrid 2020 Materials and Structures, Sankt Augustin, 2020, pp. 33–39.

[44] J. Maj, M. Basista, W. Węglewski, K. Bochenek, A. Strojny-Nędza, K. Naplocha, T. Panzner, M. Tatarková, F. Fiori, Effect of microstructure on mechanical properties and residual stresses in interpenetrating aluminum-alumina composites fabricated by squeeze casting, Mater. Sci. Eng. A (ISSN: 09215093) 715 (2018) 154–162, http://dx.doi.org/10.1016/j.msea.2017.12.091.

[45] Y. Sinchuk, S. Roy, J. Gibmeier, R. Piat, A. Wanner, Numerical study of internal load transfer in metal/ceramic composites based on freeze-cast ceramic preforms and experimental validation, Mater. Sci. Eng. A (ISSN: 09215093) 585 (2013) 10–16, http://dx.doi.org/10.1016/j.msea.2013.07.022.

[46] C. Cai, H. Geng, S. Wang, B. Gong, Z. Zhang, Microstructure evolution of AlSi10Mg(Cu) alloy related to isothermal exposure, Materials (Basel, Switzerland) (ISSN: 1996-1944) 11 (5) (2018) http://dx.doi.org/10.3390/ma11050809.

[47] DIN Deutsches Institut für Normung, Aluminium und Aluminiumlegierungen - Gussstücke - Chemische Zusammensetzung und mechanische Eigenschaften.

[48] C. Kirsch, Die theorie der elastizitat und die bedürfnisse der festigkeitslehre, Z. Des Vereines Deutscher Ingenieure 42 (1898) 797–807.

[49] Y. Chen, N. Wang, O. Ola, Y. Xia, Y. Zhu, Porous ceramics: Light in weight but heavy in energy and environment technologies, Mater. Sci. Eng.: R: Rep. (ISSN: 0927796X) 143 (2021) 100589, http://dx.doi.org/10.1016/j.mser.2020.100589.

[50] H. Horiit, S. Nemat-Nasser, Brittle failure in compression : Splitting , faulting and brittle-ductile transition, Philos. Trans. R. Soc. London 319 (1549) (1986) 337–374, [Online]. Available: https://www.jstor.org/stable/37893.

[51] V.D. Krstic, On the fracture of brittle-matrix/ductile-particle composites, Philos. Mag. A (ISSN: 0141-8610) 48 (5) (1983) 695–708, http://dx.doi.org/10.1080/01418618308236538.